Research Article
doi.org/10.1002/elsa.202300017

Chemistry Europe
European Chemical Societies Publishing

Received: 3 June 2023
Revised: 31 August 2023
Accepted: 1 September 2023

Correlation of the electronic structure and Li-ion mobility with modulus and hardness in $LiNi_{0.6}Co_{0.2}Mn_{0.2}O_2$ cathodes by combined near edge X-ray absorption finestructure spectroscopy, atomic force microscopy, and nanoindentation

Florian Hausen[1,2,4] | **Niklas Scheer**[1,2] | **Bixian Ying**[3] | **Karin Kleiner**[3]

[1]Institute of Energy and Climate Research, IEK-9, Forschungszentrum Jülich GmbH, Jülich, Germany

[2]Institute of Physical Chemistry, RWTH Aachen University, Aachen, Germany

[3]Münster Electrochemical Energy Technology (MEET), University of Münster (WWU) Corrensstraße 46, Münster, Germany

[4]Jülich Aachen Research Alliance, JARA-Energy, Jülich, Germany

Correspondence
Florian Hausen, Institute of Energy and Climate Research, IEK-9, Forschungszentrum Jülich GmbH, Jülich, Germany.
Email: f.hausen@fz-juelich.de

Karin Kleiner, Münster Electrochemical Energy Technology (MEET), University of Münster (WWU) Corrensstraße 46, 48149 Muenster, Germany.
Email: karin.kleiner@uni-muenster.de

Funding information
Federal Ministry of Education and Research (BMBF), Grant/Award Number: 03XP0231

Abstract

The electrochemical performance of cathode materials in Li-ion batteries is reflected in macroscopic observables such as the capacity, the voltage, and the state of charge (SOC). However, the physical origin of performance parameters are atomistic processes that scale up to a macroscopic picture. Thus, revealing the function and failure of electrochemical devices requires a multiscale (and -time) approach using spectroscopic and microscopic techniques. In this work, we combine near-edge X-ray absorption fine structure spectroscopy (NEXAFS) to determine the chemical binding state of transition metals in $LiNi_{0.6}Co_{0.2}Mn_{0.2}O_2$ (NCM622), electrochemical strain microscopy to understand the Li-ion mobility in such materials, and nanoindentation to relate the mechanical properties exhibited by the material to the chemical state and ion mobility. Strikingly, a clear correlation between the chemical binding, the mechanical properties, and the Li-ion mobility is found. Thereby, the significant relation of chemo-mechanical properties of NCM622 on a local and global scale is clearly demonstrated.

KEYWORDS
atomic force microscopy (ESM), correlative spectroscopy and microscopy, hardness, nanoindentation, NCM622, NEXAFS, Young's Modulus

1 | INTRODUCTION

Lithium transition metal oxides like NCMs ($LiMeO_2$ with Me = Ni_x, Co_y, Mn_z and x+y+z = 1) are state-of-the-art cathode materials in Lithium Ion Batteries (LIBs) and because of their importance, numerous scientific publications and reviews are available on these materials.[1–8] Various spectroscopic and microscopic techniques have been employed to unravel the chemical nature of the transition metals under different states of charge (SOC) as well as to gain information about topographical variations.[9–13] Near-edge X-ray absorption fine structure spectroscopy

Research Article
doi.org/10.1002/elsa.202300017
Chemistry Europe
European Chemical Societies Publishing

(NEXAFS) can be used to unravel the electronic structure of the transition metal oxides if performed on edges allowing core electrons to be excited into valence states (3d and O 2p orbitals in case of NCMs) following dipole selection rules.[14–16] By investigating the oxidation state of the active redox species (Ni in NCM622,[9]), as a function of the SOC and its distribution between the core and the rim of particles, important information about the binding nature is obtained. Variations in the electronic structure and thus in the binding state, might in turn manifest in changes in the local Li-ion diffusivity and mechanical properties of the material. To shed light on these mutual dependencies is the aim of this study.

Upon charging and discharging of the material detrimental processes such as surface morphology changes, oxygen release, and transition metal dissolution are observed.[9,17] Next to the local Li-ion mobility in cathode materials, mechanical properties are also of significant importance and need to be studied with high spatial resolution, because cracking of NCM particles under electrochemical conditions has been identified as a crucial factor for their poor cycling stability.[18] Nanoindentation offers an approach to studying the mechanical stability of NCM particles. Especially, the Zhao group has pioneered the technique with respect to battery materials.[19–22] De Vasconceloz et al. investigated NCM532 under wet and dry conditions by nanoindentation and found no significant differences between both conditions.[19] Thereby, it can be concluded that the overall lower performance of NCM cathode materials in contact with solid electrolytes over liquid electrolytes is caused by the mechanical rigidity of solid-state electrolytes. Xu et al. studied NCM532 as a function of the SOC and found a reduced Young's Modulus and Hardness with an increasing SOC.[22]

Electrodes in Li-ion batteries are not homogeneous since they are a composite of the active material, conductive carbon, and binder, as schematically illustrated in Figure 1a. As the active material undergoes severe changes upon charge and discharge, mechanical properties are of the same importance to understanding SOC-dependent functions, especially as stress, volumetric expansion, deformation, and fraction occur between the active material and the inactive support matrix upon electrochemical reactions. Furthermore, the heterogeneous distribution of the active material within the electrode might be prone to cause variations in the electronic properties of the cathodes. This will lead to limitations in the kinetics upon cycling and needs to be mapped out carefully to improve the overall performance of the electrodes.

In this work, NCM622 is chosen as a model material as it is well-characterized already and shows the highest diffusivity among various NCM materials.[23] The relation between the chemical binding state of the transition metals revealed by NEXAFS, and the mechanical properties of the material investigated with nanoindentation and correlative electrochemical strain microscopy (ESM) illustrate local Li-ion mobilities for the first time. The unique combination of different techniques provides a holistic characterization approach and demonstrates the strong correlation between (electro)chemical and mechanical behavior.

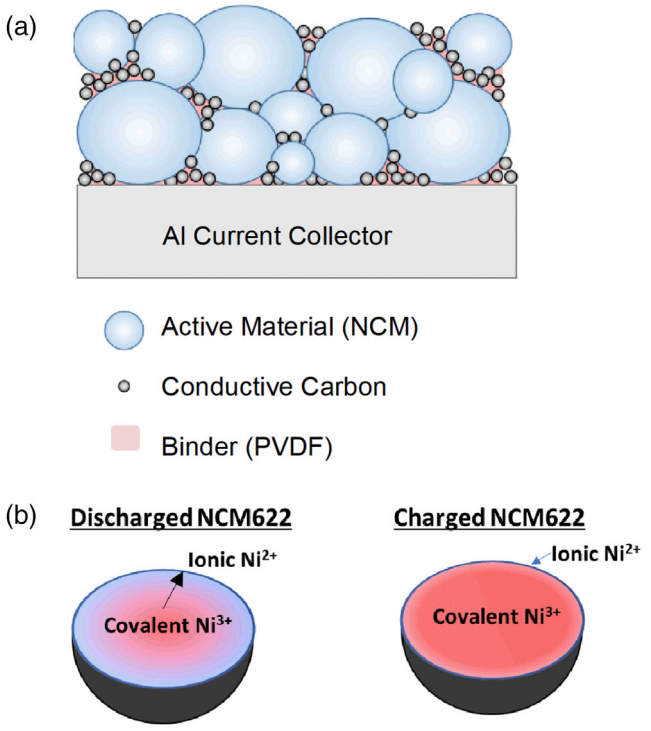

FIGURE 1 (a) Depiction of the composite structure of $LiNi_{0.6}Co_{0.2}Mn_{0.2}O_2$ (NCM622) with the active material (particles depicted as blue spheres), conductive carbon (nanoparticles depicted as dark grey spheres), and binder (PVDF) matrix in which the active material and conductive carbon are embedded (red background). The active material, conductive carbon, and binder matrix are casted on an Al foil depicted in light grey at the bottom of the picture. (b) Distribution of the chemical nature of Nickel in (dis)charged and charged NCM622 particles. While charged particles consist mainly of covalent Ni^{3+}, a significant gradient of Ni^{2+} at the rim of the particles to covalent Ni^{3+} in the core of the particles is found. On an individual particle basis, the physical properties of layered oxides such as NCM622 change upon charge and discharge because Li-ion and electron extraction lead to a higher covalence of transition metal-oxygen bonds.

2 | EXPERIMENTAL PROCEDURE

2.1 | Electrode preparation

NCM622 was synthesized as described.[9] Electrodes were prepared using 92.5 wt% cathode material (powder), 4 wt% Timcal Super C65, 3.5 wt% PVDF (Solef), and 6.5 mg of

Research Article
doi.org/10.1002/elsa.202300017
Chemistry Europe
European Chemical Societies Publishing

NMP as processing solvent. The slurry was cast on an Al foil and then dried overnight at 80°C. The obtained mass loading was approximately 14 mAh/g. For electrochemical cycling, samples with a diameter of 11 mm were punched out of the electrode sheets. The samples were dried in a Büchi oven (10^{-3} mbar, 120°C) prior to cell assembly in an argon-filled glovebox using Swagelok cells with two glass-fiber separators (diameter of 11 mm, glass microfiber 691; VWR), 60 μL of LP57 (1 M $LiPF_6$ in EC:EMC), 3:7 by weight, < 20 ppm H_2O, BASF SE) and lithium as the counter electrode (diameter of 11 mm, 99.9%; Rockwood Lithium).

2.2 | Atomic force microscopy

Five NCM622 (BASF SE) versus Li cells were charged and discharged at 0.05C (theoretical capacity of 180 mAh/g) to SOCs of 100%, 50%, and 0%, corresponding to 180, 90, and 0 mAh/g (3.0–4.3 V). To achieve smooth surfaces for the atomic force microscopy (AFM) and nanoindentation measurements, the NCM samples were mechanically polished. The NCM622 layer remained attached to the Al current collector and was fixed between two steel blocks using a clamp. This setup ensured that a cross-section of the electrode was exposed. The samples were embedded in epoxy resin (EpoFix), subsequently ground and polished with Al plates contacting the bottom. ESM experiments are obtained using a commercial atomic force microscope (Dimension Icon; Bruker) operating inside a glove box (MBraun). Cantilevers with a conductive Pt/Ir coating, nominal force constant of about 3 N/m, and nominal resonance frequency of 75 kHz (SCM-PIT-V2, Bruker and ESM, NanoSensors) were employed and calibrated individually. Slow scanning speeds between 0.1 and 0.5 Hz were chosen to ensure reliable tip–sample interaction. As the ESM results do not represent the core findings described in this manuscript the interested reader is referred to[24] for further experimental details about the ESM measurements.

2.3 | Near-edge X-ray absorption fine structure spectroscopy

The electrodes were charged and discharged with C/20 at 25°C. Samples were taken in the charged state, at 50% SOC, and in the discharged state. The cells were disassembled in an argon-filled glovebox. All samples were vacuum dried in a Büchi oven (10^{-3} mbar, 25°C) prior to the measurements without contact with air to avoid outgassing in the UHV chamber. An argon-filled transfer case was used for the sample transfer from the glovebox to the measuring chamber of the beamline. NEXAFS measurements were performed at IQMT's soft X-ray beamline WERA at the Karlsruhe synchrotron light source KARA. The photon-energy resolution in the spectra was set to 0.2–0.4 eV. Energy calibration (using a NiO reference), dark current subtraction, division by I_0, background subtraction, data normalization, and absorption correction were performed as described.[25,26] Data was collected in Fluorescence Yield (FY) and Total Electron Yield (TEY) mode, simultaneously. Absorption correction was performed as described in.[25]

2.4 | Nanoindentation

Indentation experiments have been performed employing a Hysitron Triboindenter TI980 (Bruker) under ambient conditions. A diamond indenter with a Berkovich tip shape has been employed and calibrated prior to measurements on fused quartz. Thereby, the reduced modulus (E_r) and the hardness (H) are obtained via stress-strain curves as described in the main part of the manuscript following the Oliver-Pharr method.[27] The maximal applied load was 450 μN with 0.1 s for loading, holding, and unloading, respectively for each of a total of 441 indents performed per map.

3 | RESULTS AND DISCUSSION

NCM622 is a polycrystalline powder of 5–10 μm big secondary, spherical particles that consist of 100–250 nm big, single crystallites. The particles exhibit different gradients of ionic Ni^{2+} and covalent Ni^{3+} between the outer rim of the particles and the inner core in the discharged and charged state, as depicted schematically in Figure 1b.[24] NEXAFS has been employed to verify this aspect in detail for NCM622 in the charged state, at 50% SOC, and in the discharged state to correlate the obtained results with mechanical and microscopic information. Therefore, data was measured in total electron (TEY; sampling depth of ~10 nm) and fluorescence yield mode (FY, sampling depth of ~100s nm), simultaneously. The FY data is self-absorption corrected.[28] Figure 2 shows the NEXAFS spectra (Ni L edge) from the surface near regions (TEY) and from the more bulk-like material (FY) for a), discharged, b), 50% SOC, and c), charged NCM622 particles.

When focusing on the TEY spectra of discharged NCM622 (blue dashed line, Figure 2a), pronounced Ni^{2+} peaks are observed at 853 and 871 eV (L_3/L_2 edge), respectively, while smaller peaks at 855.5 eV and 873 eV (L_3/L_2 edge) correspond to a Ni^{3+} configuration. The assignment

Research Article
doi.org/10.1002/elsa.202300017
Chemistry Europe
European Chemical Societies Publishing

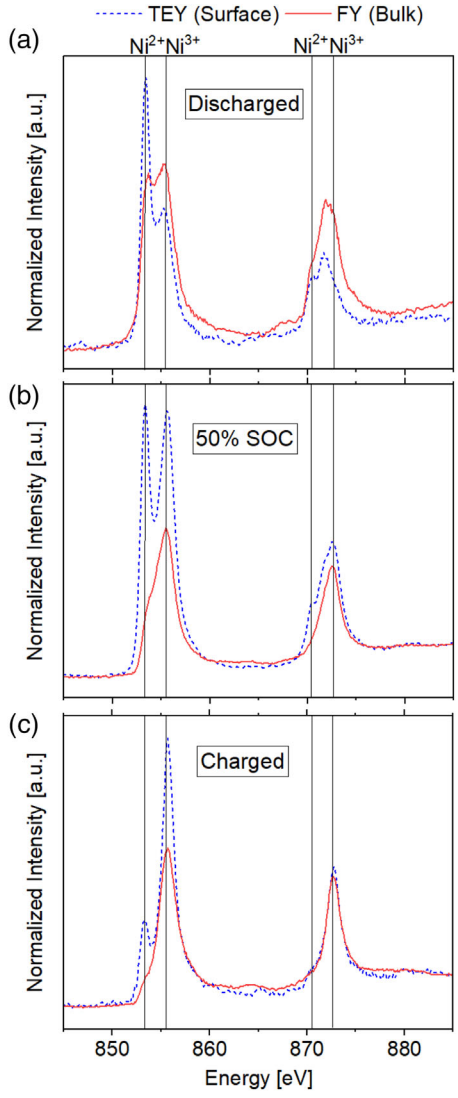

FIGURE 2 Near-edge X-ray absorption fine structure spectroscopy (NEXAFS) spectra (Ni L edge) of (a), charged $LiNi_{0.6}Co_{0.2}Mn_{0.2}O_2$ (NCM622), (b), NCM622 at 50% state of charge (SOC), and (c), discharged NCM622. The blue spectra are measured in fluorescence yield (FY), and the red spectra in total electron yield (TEY) mode.

of the peaks to individual transition metal configurations is given in [29]. While Ni^{2+} is a very ionic configuration, Ni^{3+} leads to holes in the p-band and thus to a very covalent configuration.[11,29] In comparison, the FY spectra exhibit rather similar peak intensities for both species as depicted by the red curve in Figure 2a, while the Ni^{2+} configuration is much more dominant in the TEY spectrum (blue dotted line). Although self-absorption effects may alter the spectra and cannot be completely eliminated with corrections,[28,29] the differences in the spectral weight of the Ni^{2+} and Ni^{3+} peaks measured in TEY and FY mode are significant. That the deviations are real can also be seen comparing the spectra at higher SOCs: Upon charge, the TEY and the FY spectra assimilate and the initial gradient levels off. If the differences in the TEY and FY spectra were due to self-absorption effects, the difference between the TEY and FY spectra in Figure 2a–c would remain. In the bulk material as well as at the surface, the Ni^{2+} peak drastically decreases from 0 to 100% SOC. This confirms that the particles used in this study exhibit a Ni^{2+}/Ni^{3+} gradient with a highly ionic Ni^{2+} at the rim when in the discharged state and more covalently bound Ni^{3+} in the core of the particles, in agreement with earlier work.[24,30] This gradient disappears when the particles are charged to 100% SOC.

Advanced AFM is a powerful tool to investigate cathode materials since it simultaneously provides information about the morphology, nanoelectrical, and nanomechanical properties with high spatial resolution. ESM, an AFM-based technique, has been pioneered by Balke et al.[31] and has been employed since then for different cathode[24,32–35] and anode materials,[36,37] as well as on solid-state electrolytes.[38–42] Figure 3 shows ESM results on the NCM622 particles employed in this study.

Figure 3a depicts the topography of an ensemble of NCM622 particles in the sample and reveals that the particles are partially connected to each other while others are more separated. Figure 3b shows the ESM Amplitude signal, being correlated to the local Li-ion mobility.[24] In both channels variations within individual particles are observed. However, in the ESM amplitude channel, variations between the outer part of the particles and the inner part are more pronounced. Lushta et al. studied the relation between the amplitude signal and the contact resonance frequency (CRF) in ESM and found that the exact correlation indicates the predominant excitation mechanism.[38] However, the CRF also depends critically on the tip-sample stiffness and hence, reacts very sensitively to variations in the mechanical properties of the sample such as hardness and modulus. Figure 3c illustrates the corresponding CRF image of the same position as shown in Figure 3a,b. The CRF on NCM622 is increased compared to the surrounding binder material. While individual particles exhibit a heterogeneous distribution of the CRF across the surface, the images also indicate that the outside typically shows a tendency to larger CRFs at 0% SOC. This observation implies a stiffer substrate at these locations compared to reduced contact resonances, being related to softer materials in the more central parts of the particles. Therefore, the mechanical properties of the NCM particles can be compared to the NEXAFS data that show clear evidence for alterations in the electronic structure of NCM particles between their surface areas and the bulk material as described earlier in this manuscript (cf. Figure 2). Furthermore, NEXAFS revealed that the electronic structure variations are more severe between surface and bulk structures for 0% SOC and weakest for 100% SOC.

Research Article
doi.org/10.1002/elsa.202300017
Chemistry Europe
European Chemical Societies Publishing

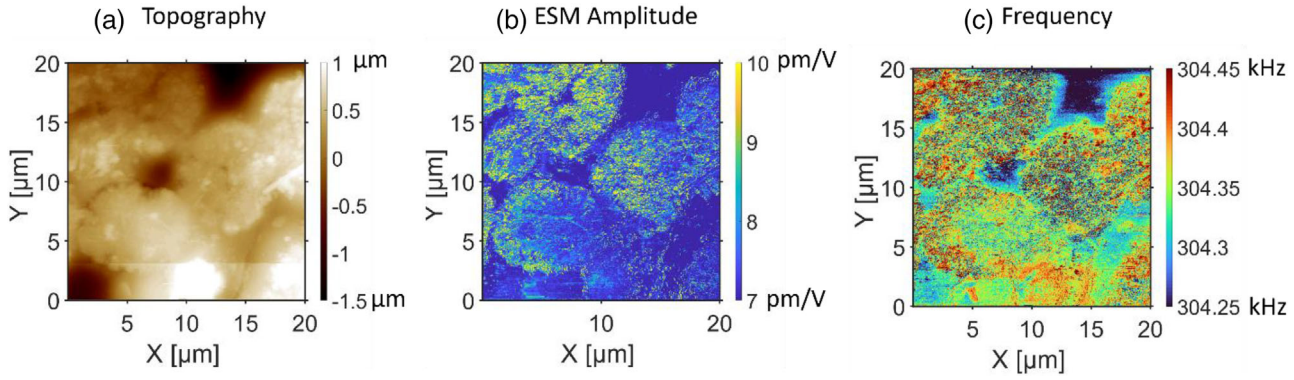

FIGURE 3 (a) Topography of an ensemble of $LiNi_{0.6}Co_{0.2}Mn_{0.2}O_2$ (NCM622) particles at 0% state of charge (SOC). (b) Simultaneously recorded ESM Amplitude imaging, revealing the local Li-ion mobility within the particles. Yellow colors indicate high mobility while blue color represents a low ESM amplitude. Clear variations are observed in individual particles. (c) Contact resonance frequency of the tip-sample contact for the same position in (a) and (b). Variations in the stiffness of the material induce variations in the observed signal. Thereby, the NCM particles can be clearly distinguished from the surrounding binder material. Although less clear than for the ESM Amplitude signal, slightly higher contact resonance frequencies (red colors) are found at the outer parts of the particles.

Figure 4 illustrates the topography and CRFs at SOCs of 0%, 50% and 100%.

Single particles are identified in the topography images, revealing similar height variations between 1 and 2 μm. As already shown in Figure 3c, the difference in CRF between the NCM622 particle and surrounding medium allows us to distinguish both materials at 0% SOC. However, this dissimilarity decreases at 50% SOC and 100% SOC and the CRF at the particle and binder material align. This observation implies that the entire NCM622 particle becomes softer at higher SOCs. Furthermore, and in agreement with the NEXAFS data (cf. Figure 2), the particles at 50% SOC and at 100% SOC do not show such a clear heterogeneity within one particle as compared to those at 0% SOC. Similarly, the Li-ion mobility is influenced as shown in an earlier report on polished as well as unpolished NCM622 cathode materials.[24] When combining both, NEXAFS and AFM, it might be concluded that the changes in electronic structure and thus, chemical bonding states are also reflected in the mechanical properties of the NCM

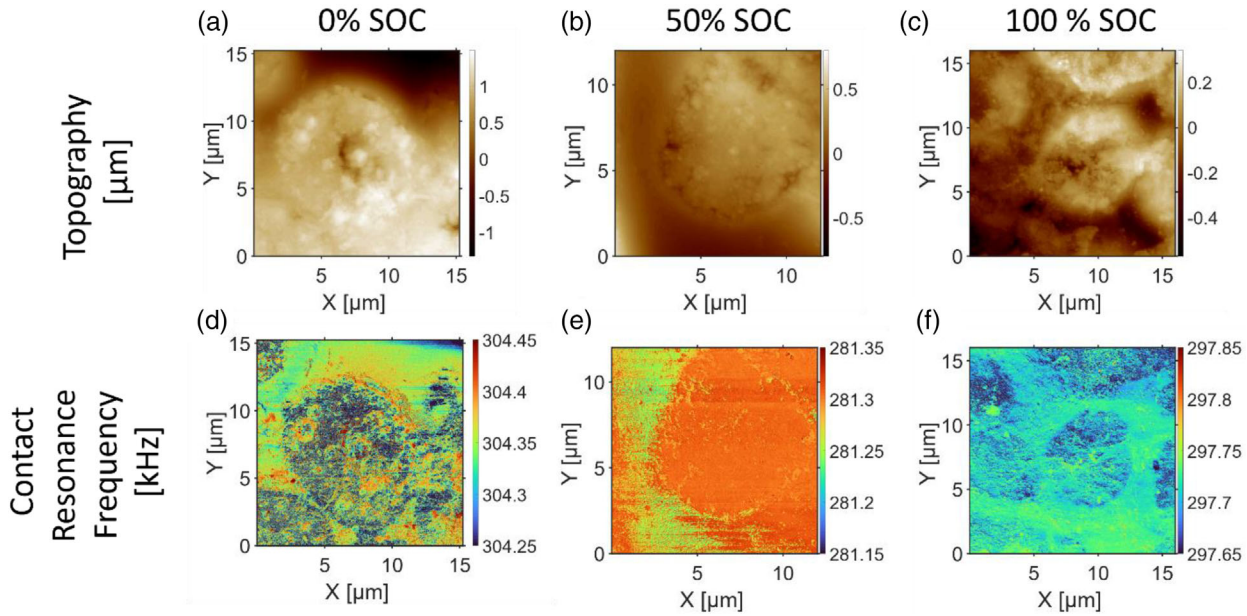

FIGURE 4 (a–c) Topography at 0%, 50%, and 100% state of charge (SOC), respectively. (d–f) Corresponding simultaneously recorded contact resonance frequency at 0%, 50%, and 100%.

Research Article
doi.org/10.1002/elsa.202300017
Chemistry Europe
European Chemical Societies Publishing

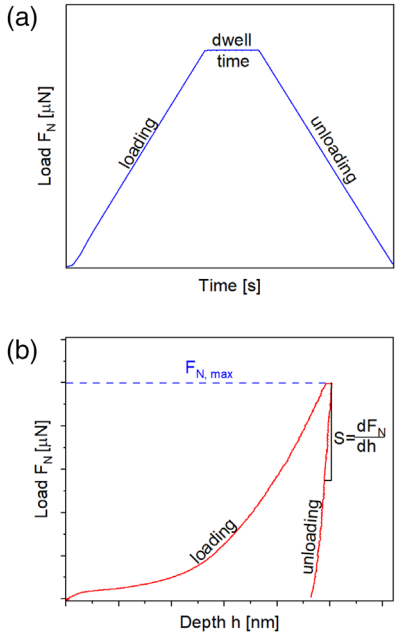

FIGURE 5 (a) Depiction of the indentation experiment: At each position, the indenter tip is pressed on the substrate for a defined time until the predefined maximum load is applied. After holding it at this load the sample is unloaded. (b) Typical load–displacement (Depth) curve from the experiment: The load is increased until the predefined load is reached, and the corresponding displacement of the tip is recorded.

particles. However, direct mechanical studies based on AFM might be subject to errors due to the compliance of the cantilever. Therefore, the AFM cantilever as well as the sample surface might undergo deformations and both signals must be deconvoluted for reliable results. The same effect makes fully quantitative experiments by AFM-based methods challenging.

In Nanoindentation a fixed tip is pressed into the sample that is not deflected itself and thus, the measured displacement is a direct response of the sample.[27,43] To study the mechanical configuration of individual NCM particles in greater detail, nanoindentation has been performed on the identical samples as have been used for NEXAFS and ESM investigations.

As nanoindentation is not a standard technique for the characterization of energy materials, Figure 5 illustrates the fundamental method. The indenter tip presses against the sample while the load and the displacement are recorded. Figure 5a shows the applied load as a function of time. The load acting on the sample is constantly increased for 0.1 s until the maximum load of 450 μN is reached. Then, the load is held for 0.1 s before the pressure is relaxed again in 0.1 s. When the load versus displacement is depicted, typical load—displacement curves, or stress-strain diagrams, as shown in Figure 5b are yielded and important parameters can be extracted: The hardness H of the sample, That is the resistance against deformation, is calculated as the maximal applied load $F_{N,max}$ divided by the contact area A. Please look at the given Equation (1) below:

$$H = \frac{F_{N,\,max}}{A} \tag{1}$$

Additionally, the reduced modulus E_r is calculated according to Equation (2), where S is the slope in the load—displacement curve when relaxing the load.

$$E_r = \frac{S\sqrt{\pi}}{2\sqrt{A}} = \frac{E_{indenter}}{1-\upsilon^2_{indenter}} + \frac{E_{sample}}{1-\upsilon^2_{sample}} \tag{2}$$

The elastic Modulus $E_{indenter}$ and Poisson ratio $\nu_{indenter}$ are 1141 GPa and 0.07, respectively.[27] As the exact value for the Poisson ratio ν_{sample} for the NCM material is not known, the conversion of E_r to Young's modulus is omitted. A value for ν_{NCM} of 0.3 has been assumed in the literature for NCM(532).[19]

Indentations have been made in a 30 x 30 μm grid of NCM622 samples with a total of 441 indents. Figure 6a provides an image of the NCM622 particles at a SOC of 0% recorded in the SPM mode of the nanoindenter, thereby revealing the topography of the sample. The image is very reminiscent of Figure 3a, obtained by AFM. Even small residues with triangular shape, resembling the shape of the indenter, are resolved on top of the NCM particles. Such a morphology is also observed by AFM (cf. Figure 3a). The difference in shape between AFM and nanoindenter is due to very different tip sizes. While the small AFM tip is capable of resolving the structure, the shape of the large indenter tip is mirrored. However, it is clearly verified that the indenter is also capable of revealing images with a spatial resolution that allows to identify individual NCM particles. Furthermore, the image depicted in Figure 6a provides the basis to perform indentations every 1.5 μm. From the individual indents color maps of the reduced modulus E_r and hardness H are extracted and presented in Figure 6b,c. An influence of the small particles on top of the NCM particles is not discernible and thus, not expected due to the dimensions of each indent.

Individual NCM particles can be identified based on the distribution shown in Figure 6a. The particles exhibit an increased E_r and H compared to the positions between them. Interestingly, pronounced variations at the rim of NCM622 particles compared to their inner regions are observed, both in E_r and H. Compared to the Li-ion mobility investigated by ESM and CRF shown in Figure 3b,c the similarity is striking. Additionally, it verifies the observation by the contact resonance frequency and indicates

Research Article
doi.org/10.1002/elsa.202300017
Chemistry Europe
European Chemical Societies Publishing

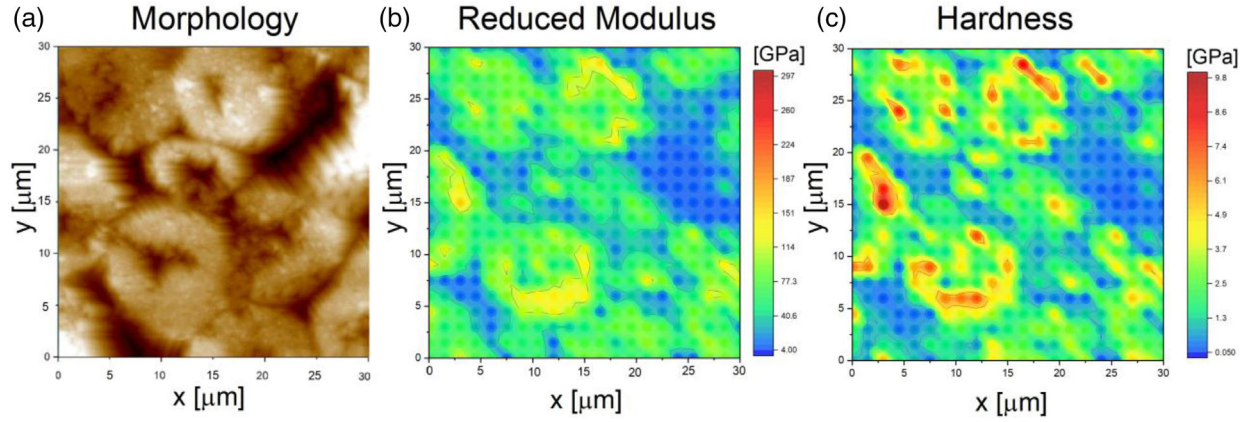

FIGURE 6 (a) Morphology of the area where the indentation experiment on $LiNi_{0.6}Co_{0.2}Mn_{0.2}O_2$ (NCM622) @ 0% state of charge (SOC) was conducted afterwards. (b) Reduced Modulus map and (c) calculated Hardness map at the position shown in (a). A clear variation at the rims of the particles is observed, exhibiting a higher reduced modulus as well as a higher hardness.

variations between the inner and outer regions of individual particles. However, the differences are far more pronounced in the quantitative nanoindentation experiments than in the contact resonance frequency maps in AFM, although AFM provides a higher spatial resolution. This is probably related to the significantly larger indentation depth in nanoindentation compared to the direct tip-surface interaction in AFM. Furthermore, it seems that the size of the individual NCM particles influences the overall gradient, as the particles towards the lower right and in the center of the region under investigation do not exhibit such high values at their rim in comparison to the larger particles on the top and left. However, it might be that those particles show a slightly reduced E_r at the rim as well as in the middle of the particle and hence, still display a gradient from the outside to the inside. Such a gradient is also found in the NEXAFS experiment, although the information depth for TEY showing the higher Ni^{2+} content is rather limited to the initial ~10 nm and hence, cannot be quantified in the mechanical experiments. However, the NEXAFS data clearly reveal a fading off the gradient as a function of SOC. For 100% SOC the difference in the electronic states between the bulk material and the surface is vanished. To verify that the mechanical properties of NCM622 are directly related to the electronic structure, respectively the Ni oxidation state, mechanical properties are also quantified as a function of SOC. Figure 7 displays the reduced modulus of individual NCM622 particles at 0 %, 50 % and 100 % SOC.

Figure 7a is the same as in Figure 6b and shows the situation at 0% SOC. With increasing the SOC to 50% the particles still exhibit a significantly increased E_r compared to the binder material, but do not show a distinct variation between the outside and the core of the particles. Please note that the respective positions are not identical between different images. At 100% SOC, no particles can be identified based on their reduced modulus. That this effect of reduced E_r and more homogeneous distribution across individual particles is indeed due to the particles is confirmed by the E_r values of the binder that remain almost unchanged as a function of SOC. Table 1 provides different statistical data and the exact values obtained from the nanoindentation maps depicted in Figure 7. As the NEXAFS data presented in Figure 2 also supports a more homogeneous distribution between Ni^{2+} and Ni^{3+} within the charged NCM622, a close correlation between the electronic structure of the cathode active material and the mechanical properties is evident. Ni^{2+}, predominantly located at the rim of the particles, exhibits an ionic nature, while Ni^{3+} shows a more covalent character.[9]

The obtained hardness maps of the NCM622 at different SOCs are shown in Figure 8.

In agreement with the observations made for E_r the hardness of the binder material is not changing as a function of SOC. Table 2 provides different statistical data and the exact values obtained from the nanoindentation maps depicted in Figure 7. However, the strong gradient at 0% SOC within individual particles diminishes at 50% SOC and no particles can be identified anymore at 100% SOC

TABLE 1 Summary of statistical values obtained from the data shown in Figure 7. All values in [GPa].

Reduced modulus	SOC 0%	SOC 50%	SOC 100%
Mean Value	55.99	37.66	23.70
Maximum	155.77	296.58	85.12
Minimum	7.25	4.26	4.69
Standard Deviation	33.92	26.07	11.85
75% Percentile	82.38	54.28	30.39
50% Percentile	52.66	32.77	21.25
25% Percentile	26.66	17.84	14.74

Research Article
doi.org/10.1002/elsa.202300017
Chemistry Europe
European Chemical Societies Publishing

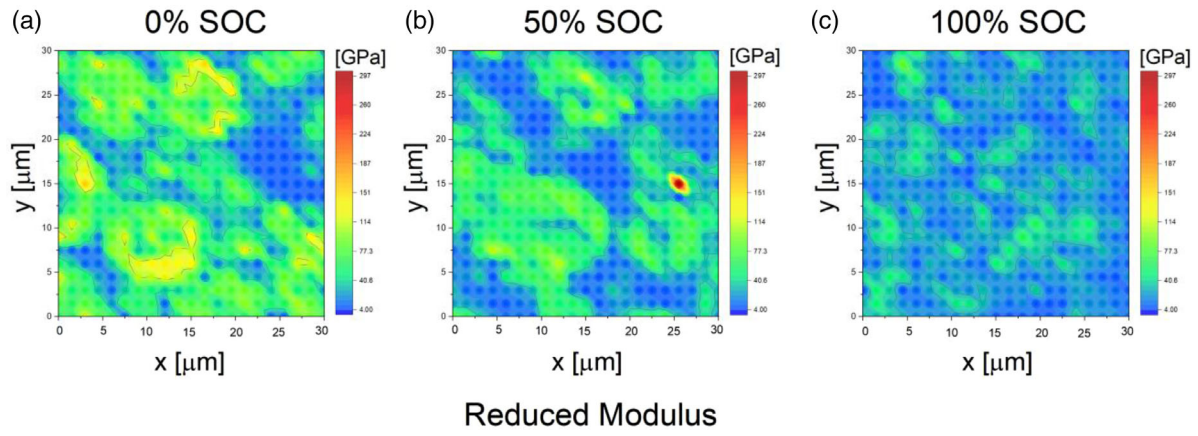

FIGURE 7 Color maps of the obtained E_r for (a) 0% state of charge (SOC), (b) 50% SOC, and (c) 100% SOC. It is important to note that the images are obtained from different regions of the respective samples. At 50% SOC, the pronounced differences between the rim and the core of the particles diminish, but $LiNi_{0.6}Co_{0.2}Mn_{0.2}O_2$ (NCM622) still exhibits an increased E_r compared to the binder material. At 100% SOC, no particles can be identified from the reduced modulus map anymore.

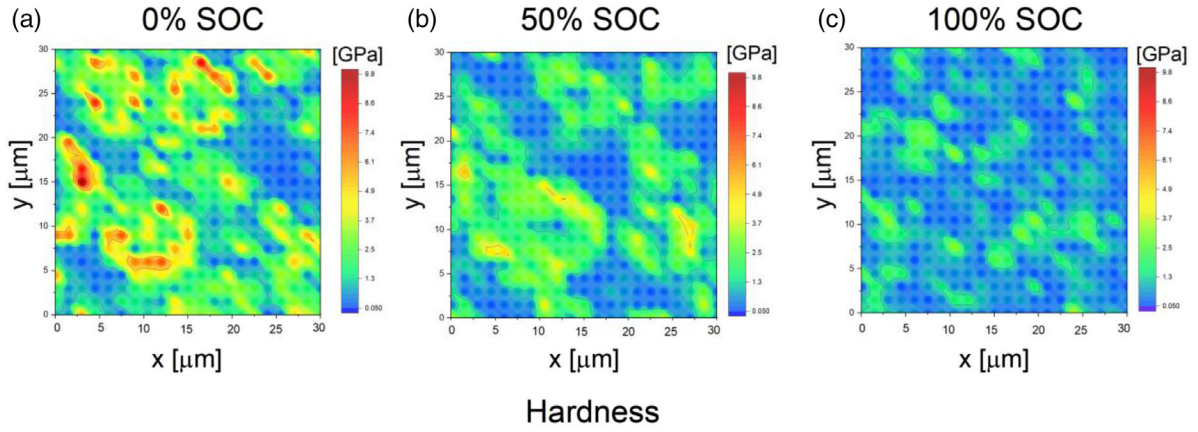

FIGURE 8 Color maps of the obtained H for (a) 0% state of charge (SOC), (b) 50% SOC, and (c) 100% SOC. It is important to note that the images are obtained from different regions of the respective samples. A severe gradient is observed within the $LiNi_{0.6}Co_{0.2}Mn_{0.2}O_2$ (NCM622) particles at 0% SOC between the outside and the center. At 50% SOC, the pronounced differences diminish, but NCM622 still exhibits an increased H compared to the binder material. At 100% SOC, no particles can be identified from the hardness map anymore.

as depicted in Figure 8c). This finding clearly supports the interpretation of a more ionic species, namely Ni^{2+} at the rim of NCM622 particles in the discharged state (0% SOC) and more covalently bound Ni^{3+} towards the center of the particles as well as a decrease of Ni^{2+} species with higher SOCs (cf. Figure 1b). This is also verified by the NEXAFS results shown in Figure 2 as well as indicated by the contact resonance frequency shift, observed in AFM-based experiments (cf. Figure 4).

TABLE 2 Summary of statistical values obtained from the data shown in Figure 8. All values in [GPa].

Hardness	SOC 0%	SOC 50%	SOC 100%
Mean Value	2.12	1.42	0.79
Maximum	9.77	5.15	3.68
Minimum	0.07	0.14	0.08
Standard Deviation	1.73	1.08	0.63
75% Percentile	2.99	1.98	1.01
50% Percentile	1.53	1.11	0.57
25% Percentile	0.78	0.52	0.34

The obtained mean values for reduced modulus and hardness are depicted in Figure 9 for the individual SOCs and taken from the entire image, that is, NCM622 particles and surrounding binder. Thus, due to the gradient found at 0% SOC (fully lithiated) and the clear difference in mechanical properties between the binder material and the NCM622 particles, the error bars are larger than for 100% SOC.

Interestingly, the differences in reduced modulus and hardness between the different SOCs are severe, especially when considering that the binder does not change its mechanical values and hence, the hardness and reduced modulus for NCM622 at 0% SOC is rather underestimated.

Research Article
doi.org/10.1002/elsa.202300017
Chemistry Europe
European Chemical Societies Publishing

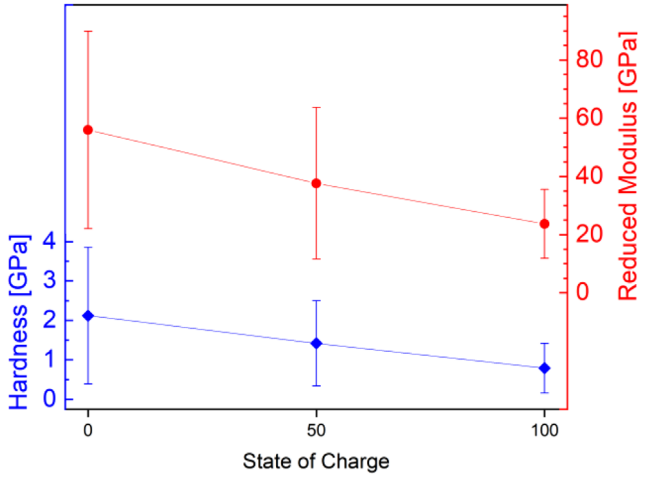

FIGURE 9 Summary of the found values for hardness and reduced modulus for $LiNi_{0.6}Co_{0.2}Mn_{0.2}O_2$ (NCM622) particles and surrounding binder material as a function of state of charge (SOC). Error bars correspond to the standard deviation.

Clearly, such mechanical alterations must be considered when discussing the formation of cracks upon charge and discharge in a real battery, particularly since the matrix does not behave accordingly.

Although the trend seems to indicate a linear relationship between Hardness/reduced modulus and SOC, a closer inspection reveals that the drop is slightly overproportional between 0% and 50% compared to 50% and 100%. However, this trend is in clear accordance with ESM data, representing the Li-ion mobility, as reported by Jetybayeva et al. for the same NCM particles.[24] The decreasing hardness and reduced modulus with an increasing SOC are concomitant with the decreasing ionic character of the electronic structure of NCM622. Thus, a correlation between electronic and mechanical properties appears evident. Further experiments need to verify this relation.

4 | CONCLUSION

For the first time, a close link between the electronic structure of NCM622 and its mechanical behavior is demonstrated in this work. Nanoindentation of NCM622 particles as a function of the state of charge clearly verifies a strongly heterogeneous character at 0% SOC, exhibiting a much higher hardness and increased reduced modulus at the surface of the particles compared to the inner part. ESM measurements of the same samples demonstrate that also the Li-ion mobility is influenced in a similar way. This observation might be attributed to the gradient in the electronic structure of the NCM622 from outer to inner parts of the NCM particles as revealed with NEXAFS spectroscopy, although the experimental length scales are not identical. The relation is further supported by the behavior of different SOCs, leading to rather homogeneous structures and almost no differences in mechanical properties between NCM622 and surrounding binders at high SOCs. NEXAFS and AFM also reveal that the gradient between the inner and the outer part of the particles levels off with an increasing SOC. The correlative approach of microscopy (ESM, Li-ion mobility), spectroscopy (NEXAFS, electronic structure), and indentation (Quantitative mechanical information) represents a new diagnostic approach and will pave the way to a more holistic picture of processes in energy materials.

ACKNOWLEDGMENTS

The authors are grateful to Ude Hangen, Bruker Nano GmbH for experimental support as well as Stefan Schuppler, Peter Nagel, and Michael Merz, IQMT, Karlsruhe Institute of Technology for their support with the NEXAFS measurements. Moreover, our gratitude is extended to the KNMF (KIT, Germany) for the provision of beamtime. FH and NS thank Rüdiger-A. Eichel and L.G.J. (Bert) de Haart for continuous support. The NEXAFS studies were partially funded by the Federal Ministry of Education and Research (BMBF) under the funding number 03XP0231.

CONFLICT OF INTEREST STATEMENT

The authors declare no conflict of interest.

DATA AVAILABILITY STATEMENT

The data that support the findings of this study are available from the corresponding authors upon reasonable request.

ORCID

Florian Hausen https://orcid.org/0000-0001-5712-6761

REFERENCES

1. A. Chakraborty, S. Kunnikuruvan, M. Dixit, D. T. Major, *Israel J. Chem.* **2020**, *60*, 850. https://doi.org/10.1002/ijch.201900116.
2. L. de Biasi, B. Schwarz, T. Brezesinski, P. Hartmann, J. Janek, H. Ehrenberg, *Adv. Mater.* **2019**, *31*, 1900985. https://doi.org/10.1002/adma.201900985.
3. M. Jiang, D. L. Danilov, R. A. Eichel, P. H. L. Notten, *Adv. Energy Mater.* **2021**, *11*. https://doi.org/10.1002/aenm.202103005.
4. C.-H. Jung, H. Shim, D. Eum, S.-H. Hong, *J. Kor. Ceram. Soc.* **2020**, *58*, 1. https://doi.org/10.1007/s43207-020-00098-x.
5. P. K. Nayak, E. M. Erickson, F. Schipper, T. R. Penki, N. Munichandraiah, P. Adelhelm, H. Sclar, F. Amalraj, B. Markovsky, D. Aurbach, *Adv. Energy Mater.* **2018**, *8*, 1702397. https://doi.org/10.1002/aenm.201702397.

6. Y. Dong, J. Li, *Chem. Rev.* **2023**, *123*, 811. https://doi.org/10.1021/acs.chemrev.2c00251.
7. R. Jung, M. Metzger, F. Maglia, C. Stinner, H. A. Gasteiger, *J. Electrochem. Soc.* **2017**, *164*, A1361. https://doi.org/10.1149/2.0021707jes.
8. S. Schweidler, L. de Biasi, G. Garcia, A. Mazilkin, P. Hartmann, T. Brezesinski, J. Janek, *ACS Appl. Energy Mater.* **2019**, *2*, 7375. https://doi.org/10.1021/acsaem.9b01354.
9. K. Kleiner, C. A. Murray, C. Grosu, B. Ying, M. Winter, P. Nagel, S. Schuppler, M. Merz, *J. Electrochem. Soc.* 120533, **2021**, *168*. https://doi.org/10.1149/1945-7111/ac3c21.
10. Y. Koyama, I. Tanaka, H. Adachi, Y. Makimura, T. Ohzuku, *J. Power Sources* **2003**, *119-121*, 644. https://doi.org/10.1016/S0378-7753(03)00194-0.
11. L. A. Montoro, M. Abbate, J. M. Rosolen, *J. Electrochem. Soc.* **2000**, *147*, 1651. https://doi.org/10.1149/1.1393412.
12. L. A. Montoro, J. M. Rosolen, *Electrochim. Acta* **2004**, *49*, 3243. DOI https://doi.org/10.1016/j.electacta.2004.03.001.
13. W.-S. Yoon, M. Balasubramanian, K. Y. Chung, X.-Q. Yang, J. McBreen, C. P. Grey, D. A. Fischer, *J. Am. Chem. Soc.* **2005**, *127*, 17479. https://doi.org/10.1021/ja0530568.
14. F. de Groot, A. Kotani, *Core Level Spectroscopy of Solids*, CRC Press, Boca Raton, FL **2008**.
15. K. Kleiner, H. Ehrenberg, *Top Curr. Chem.* **2017**, *375*, 54. https://doi.org/10.1007/s41061-017-0139-2.
16. K. Kleiner, J. Melke, M. Merz, P. Jakes, P. Nagel, S. Schuppler, V. Liebau, H. Ehrenberg, *ACS Appl. Mater. Interfaces* **2015**, *7*, 19589. https://doi.org/10.1021/acsami.5b03191.
17. M. Merz, B. Ying, P. Nagel, S. Schuppler, K. Kleiner, *Chem. Mater.* **2021**, *33*, 9534. https://doi.org/10.1021/acs.chemmater.1c02573.
18. R. Ruess, S. Schweidler, H. Hemmelmann, G. Conforto, A. Bielefeld, D. A. Weber, J. Sann, M. T. Elm, J. Janek, *J. Electrochem. Soc.* **2020**, *167*, 100532. https://doi.org/10.1149/1945-7111/ab9a2c.
19. L. S. de Vasconcelos, N. Sharma, R. Xu, K. Zhao, *Exp. Mech.* **2018**, *59*, 337. https://doi.org/10.1007/s11340-018-00451-6.
20. L. S. de Vasconcelos, R. Xu, K. Zhao, *J. Electrochem. Soc.* **2017**, *164*, A3840. https://doi.org/10.1149/2.1411714jes.
21. N. Sharma, D. Meng, X. Wu, L. S. de Vasconcelos, L. Li, K. Zhao, *Extreme Mech. Lett.* **2023**, *58*, 101920. https://doi.org/10.1016/j.eml.2022.101920.
22. R. Xu, H. Sun, L. S. de Vasconcelos, K. Zhao, *J. Electrochem. Soc.* **2017**, *164*, A3333. https://doi.org/10.1149/2.1751713jes.
23. S. Cui, Y. Wei, T. Liu, W. Deng, Z. Hu, Y. Su, H. Li, M. Li, H. Guo, Y. Duan, W. Wang, M. Rao, J. Zheng, X. Wang, F. Pan, *Adv. Energy Mater.* **2016**, *6*, 1501309. https://doi.org/10.1002/aenm.201501309.
24. A. Jetybayeva, N. Schön, J. Oh, J. Kim, H. Kim, G. Park, Y.-G. Lee, R.-A. Eichel, K. Kleiner, F. Hausen, S. Hong, *ACS Appl. Energy Mater.* **2022**, *5*, 1731. https://doi.org/10.1021/acsaem.1c03173.
25. M. Merz, P. Nagel, C. Pinta, A. Samartsev, H. V. Löhneysen, M. Wissinger, S. Uebe, A. Assmann, D. Fuchs, S. Schuppler, *Phys. Rev. B* **2010**, *82*, 174416. https://doi.org/10.1103/PhysRevB.82.174416.
26. M. Merz, D. Fuchs, A. Assmann, S. Uebe, H. V. Löhneysen, P. Nagel, S. Schuppler, *Phys. Rev. B* **2011**, *84*, 014436. https://doi.org/10.1103/PhysRevB.84.014436.
27. W. C. Oliver, G. M. Pharr, *J. Mater. Res.* **1992**, *7*, 1564. https://doi.org/10.1557/JMR.1992.1564.
28. L. Tröger, D. Arvanitis, K. Baberschke, H. Michaelis, U. Grimm, E. Zschech, *Phys. Rev. B* **1992**, *46*, 3283. https://doi.org/10.1103/PhysRevB.46.3283.
29. K. Kleiner, C. A. Murray, C. Grosu, S. J. Day, M. Winter, P. Nagel, S. Schuppler, M. Merz, *Cation. Anion. Redox.* **2020** https://arxiv.org/abs/2006.09964
30. K. Kleiner, D. Dixon, P. Jakes, J. Melke, M. Yavuz, C. Roth, K. Nikolowski, V. Liebau, H. Ehrenberg, *J. Power Sources* **2015**, *273*, 70. https://doi.org/10.1016/j.jpowsour.2014.08.133.
31. N. Balke, S. Jesse, A. N. Morozovska, E. Eliseev, D. W. Chung, Y. Kim, L. Adamczyk, R. E. Garcia, N. Dudney, S. V. Kalinin, *Nat. Nanotechnol.* **2010**, *5*, 749. https://doi.org/10.1038/nnano.2010.174.
32. D. O. Alikin, A. V. Ievlev, S. Y. Luchkin, A. P. Turygin, V. Y. Shur, S. V. Kalinin, A. L. Kholkin, *Appl. Phys. Lett.* **2016**, *108*, 113106. https://doi.org/10.1063/1.4943944.
33. D. O. Alikin, K. N. Romanyuk, B. N. Slautin, D. Rosato, V. Y. Shur, A. L. Kholkin, *Nanoscale* **2018**, *10*, 2503. https://doi.org/10.1039/c7nr08001h.
34. N. Balke, S. Kalnaus, N. J. Dudney, C. Daniel, S. Jesse, S. V. Kalinin, *Nano Lett.* **2012**, *12*, 3399. https://doi.org/10.1021/nl300219g.
35. J. Zhu, L. Lu, K. Zeng, *ACS Nano* **2013**, *7*, 1666. https://doi.org/10.1021/nn305648j.
36. N. Balke, S. Jesse, Y. Kim, L. Adamczyk, A. Tselev, I. N. Ivanov, N. J. Dudney, S. V. Kalinin, *Nano Lett* **2010**, *10*, 3420. https://doi.org/10.1021/nl101439x.
37. M. Simolka, C. Heim, K. A. Friedrich, R. Hiesgen, *J. Electrochem. Soc.* **2019**, *166*, A5496. https://doi.org/10.1149/2.0711903jes.
38. V. Lushta, S. Bradler, B. Roling, A. Schirmeisen, *J. Appl. Phys.* **2017**, *121*, 224302. https://doi.org/10.1063/1.4984831.
39. N. Schon, D. C. Gunduz, S. Yu, H. Tempel, R. Schierholz, F. Hausen, *Beilstein J. Nanotechnol.* **2018**, *9*, 1564. https://doi.org/10.3762/bjnano.9.148.
40. N. Schon, R. Schierholz, S. Jesse, S. Yu, R. A. Eichel, N. Balke, F. Hausen, *Small Methods* **2021**, *5*, e2001279. https://doi.org/10.1002/smtd.202001279.
41. S. Sasano, R. Ishikawa, I. Sugiyama, T. Higashi, T. Kimura, Y. H. Ikuhara, N. Shibata, Y. Ikuhara, *Appl. Phys. Express* **2017**, *10*, 061102. https://doi.org/10.7567/APEX.10.061102.
42. Z. Wang, M. Kotobuki, L. Lu, K. Zeng, *Electrochim. Acta* **2020**, *334*, 135553. https://doi.org/10.1016/j.electacta.2019.135553.
43. A. C. Fischer-Cripps, D. W. Nicholson, *Appl. Mech. Rev.* **2004**, *57*, B12. https://doi.org/10.1115/1.1704625.

How to cite this article: F. Hausen, N. Scheer, B. Ying, K. Kleiner, *Electrochem. Sci. Adv.* **2024**, *4*, e2300017. https://doi.org/10.1002/elsa.202300017